

Postemplacement dynamics of basaltic intrusions in the continental crust

A. Roman, C. Jaupart

▶ **To cite this version:**

A. Roman, C. Jaupart. Postemplacement dynamics of basaltic intrusions in the continental crust. Journal of Geophysical Research : Solid Earth, 2017, 122, pp.966-987. 10.1002/2016JB013912 . insu-03748876

HAL Id: insu-03748876

https://insu.hal.science/insu-03748876

Submitted on 10 Aug 2022

HAL is a multi-disciplinary open access archive for the deposit and dissemination of scientific research documents, whether they are published or not. The documents may come from teaching and research institutions in France or abroad, or from public or private research centers.

L'archive ouverte pluridisciplinaire **HAL**, est destinée au dépôt et à la diffusion de documents scientifiques de niveau recherche, publiés ou non, émanant des établissements d'enseignement et de recherche français ou étrangers, des laboratoires publics ou privés.

Copyright

AGU PUBLICATIONS

JGR

Journal of Geophysical Research: Solid Earth

RESEARCH ARTICLE
10.1002/2016JB013912

Key Points:
- Laboratory experiments are performed to study the postemplacement dynamics of mafic intrusions
- The intrusion final aspect ratio is controlled by one dimensionless parameter
- Buoyancy reversal due to crystallization leads to foundering of the intrusion

Correspondence to:
A. Roman,
roman@ipgp.fr

Citation:
Roman, A., and C. Jaupart (2017), Postemplacement dynamics of basaltic intrusions in the continental crust, *J. Geophys. Res. Solid Earth*, *122*, 966–987, doi:10.1002/2016JB013912.

Received 29 DEC 2016
Accepted 22 JAN 2017
Accepted article online 6 FEB 2017
Published online 16 FEB 2017

©2017. American Geophysical Union. All Rights Reserved.

Postemplacement dynamics of basaltic intrusions in the continental crust

A. Roman[1] **and C. Jaupart**[1]

[1] Institut de Physique du Globe de Paris, Sorbonne Paris Cité, Université Paris Diderot, CNRS (UMR 7154), Paris, France

Abstract Laboratory experiments document the postemplacement behavior of mafic intrusions that spread at a density interface and founder as they become denser than their surroundings due to cooling and crystallization. All else being equal, the larger the intrusion volume, the farther the intrusion can spread and the smaller its aspect ratio is. The final aspect ratio is a function of a single dimensionless number analogous to the Rayleigh number of thermal convection. Once it is denser than its surroundings, the intrusion becomes unstable and may founder in two different regimes. At aspect ratios larger than about 0.4, the "teardrop" regime is such that the intrusion thickens in a central region, developing the shapes of a funnel and a pendant drop. At lower aspect ratios, another regime is observed, with thickening of the intrusion at the leading edge and thinning in a central region. The thick outer ring in turn becomes unstable into a set of teardrops and leads to an irregular horizontal outline. In one variant called the "jellyfish" regime, the thin central region develops a number of downwellings and upwellings in a Rayleigh-Taylor-like pattern. These instabilities may get arrested due to cooling as the intrusion and encasing rocks become too strong to deform. One would then be left with a funnel-shaped residual body or a wide irregular one with thick peripheral lobes and a thinner central region. These different patterns can be recognized in upper crustal mafic intrusions.

1. Introduction

Mafic and ultramafic igneous bodies come in a wide range of dimensions and shapes. Most of them are basin shaped with a thicker central area or funnel shaped without a well-defined floor [*Wager and Brown*, 1968]. Igneous layers can be traced across them in many cases but can be discontinuous in some. The Bushveld Complex, South Africa, for example, has thick peripheral lobes displaying a well-defined basal igneous sequence that is missing from the thinner central area [*Cawthorn and Webb*, 2001; *Webb et al.*, 2004; *Cole et al.*, 2014]. There are also marked differences of horizontal planforms, from the nearly circular 80 km wide Sept-Iles intrusion, Quebec [*Loncarevic et al.*, 1990], to the lobate approximately 65,000 km^2 Bushveld Complex [*Cawthorn*, 2015]. The geometrical characteristics of an intrusion plays a key role in the thermal evolution and fractional crystallization behavior of magma. Thickness determines the cooling regime, the likelihood of convective motions in the molten interior, and the efficiency of crystal/melt separation processes, whereas the aspect ratio sets the relative importance of crystallization at the side walls, floor, and roof. Understanding how and when the final geometrical characteristics have been acquired is therefore a major issue.

Basaltic parent melts rise through the crust due to buoyancy and accumulate either at a neutral buoyancy level or at an interface between different rocks, such that emplacement proceeds with a rather small density contrast between magma and host rocks, typically less than 100 kg m^{-3} [*Taisne and Jaupart*, 2009; *Roman and Jaupart*, 2016]. For almost all basaltic compositions, the bulk density of partially crystallized magma increases with increasing degree of solidification. In large reservoirs, magma does not evolve along a closed-system liquid line of descent due to crystal settling or flotation, compositional convection within thick cumulate piles, and replenishment and withdrawal through eruptions. There is no doubt, however, that the bulk intrusion eventually becomes denser than its host rocks, as shown by the large positive gravity anomalies that are generated [*Podmore and Wilson*, 1987; *Loncarevic et al.*, 1990; *Cole et al.*, 2014]. The famous Rum intrusion, Western Scotland, for example, is associated with an ≈75 mGal positive anomaly [*Emeleus et al.*, 1996]. There is therefore a marked change of density contrast between intrusion and host, which typically goes from small negative values to larger positive ones. Whether or not such large loads can be supported by crustal rocks depends on the dimensions and shape of the body. For example, a very thin and long sill is more stable than a spherical

pluton with the same total volume. One may expect that an intrusion deforms as its density increases, going from an emplacement-controlled shape to a postemplacement one. The basin structure of many mafic intrusions (lopoliths) have indeed been attributed to late sagging, indicating that encasing rocks did deform by significant amounts. This issue is of critical importance for the formation of continental crust, which results from the fractional crystallization of basaltic melts followed by the foundering of mafic cumulates [*Arndt and Goldstein*, 1989; *Kay and Mahlburg-Kay*, 1991; *Rudnick and Fountain*, 1995; *Jull and Kelemen*, 2001]. Some mafic cumulates do get preserved, and we may suspect that total loss and total preservation are two end-member situations and that in some circumstances, foundering does not proceed to completion, leaving a residual body that provides a record of the processes involved.

Studies of large igneous intrusions have focused mostly on the physical and petrological processes that are active in a basaltic melt body that is cooling down and solidifies [*Wager and Brown*, 1968; *Latypov*, 2015]. It has usually been assumed that the shape of an intrusion has been set during emplacement and has not been modified afterward. The possibility that its present shape has been acquired in a postemplacement phase has seldom been entertained and is addressed in this work. We study in the laboratory a simple model of an intrusion that becomes denser than its host as it cools down. We do not deal with the emplacement process itself, which probably involves a protracted sequence of individual magma inputs [*Sisson et al.*, 1996; *Annen and Sparks*, 2002; *Michaut and Jaupart*, 2006], and focus on the behavior of a fully formed intrusion. We thus restrict ourselves to postemplacement dynamics in a thermally mature system where encasing rocks have been heated by repeated magma injections. Our experiments involve Newtonian liquids and cannot be taken as faithful representations of geological conditions, but they allow a clear description of some of the main mechanisms at work as well as useful physical arguments involving a small number of control variables. They show that intrusions may behave in unexpected ways even in simple conditions and generate structures of great interest. To the best of our knowledge, such structures have never been described before and account for the different shapes of mafic intrusions, including the lobate outline of the Bushveld Complex. We argue that two different types of postemplacement processes may be important. A fully formed intrusion may spread laterally over significant distances as it is actively cooling down and may then founder when it becomes denser than encasing rocks due to the formation of a thick mafic cumulate pile. Its aspect ratio (thickness over radius) can be related to a single dimensionless number that depends on its volume and on the effective viscosity of the host fluids. Extrapolation to geological conditions shows that model requirements are consistent with available constraints on crustal rheology. We begin the paper with a short description of salient features of mafic and ultramafic igneous complexes and discuss how one can separate emplacement and postemplacement processes. This is followed by a summary of our experimental results and by some theoretical arguments. We return to geological conditions and observations in a final section.

2. Geological Background

2.1. Density and Buoyancy Changes in Basaltic Intrusions

Basaltic magmas, with densities in a 2600 – 2750 kg m^{-3} range at the liquidus, are buoyant with respect to most continental crustal rocks, which explains why they are often able to rise to shallow depths. Following emplacement in colder country rock, magmas cool down and crystallize, however, which leads to large changes of density.

Density values for basaltic melts and magmas are compared to those of surrounding crustal rocks in Figure 1. We have first considered a generic average tholeiitic composition (residual glass HK#19 [*Hirose and Kushiro*, 1993]) in the dry limit as well as with 2 wt % water and calculated how its density varies with pressure at the liquidus and at the (FMQ) Fayaite Magnetite Quartz redox buffer using the MELTS model [*Ghiorso and Sack*, 1995; *Asimow and Ghiorso*, 1998]. These density values are compared to an average crustal density distribution from *Christensen and Mooney* [1995]. It may be seen that the dry basalt becomes denser than average crust at midcrustal depths, implying that it is likely to stall there. In contrast, a water-rich basalt is likely to rise to the surface. We have also considered the parent magma of the famous Rum intrusion, Scotland, which was emplaced at shallow depth at the interface between Archean Lewisian crystalline basement and a younger sedimentary cover [*Emeleus et al.*, 1996; *Emeleus and Troll*, 2014]. We have calculated how the densities of both partially crystallized magma and phenocryst assemblage vary with temperature in the crystallization interval. This closed-system calculation does not account for the many processes that may occur in a large magma reservoir and is only meant to illustrate the density change and buoyancy reversal that affects a basaltic intrusion as it crystallizes.

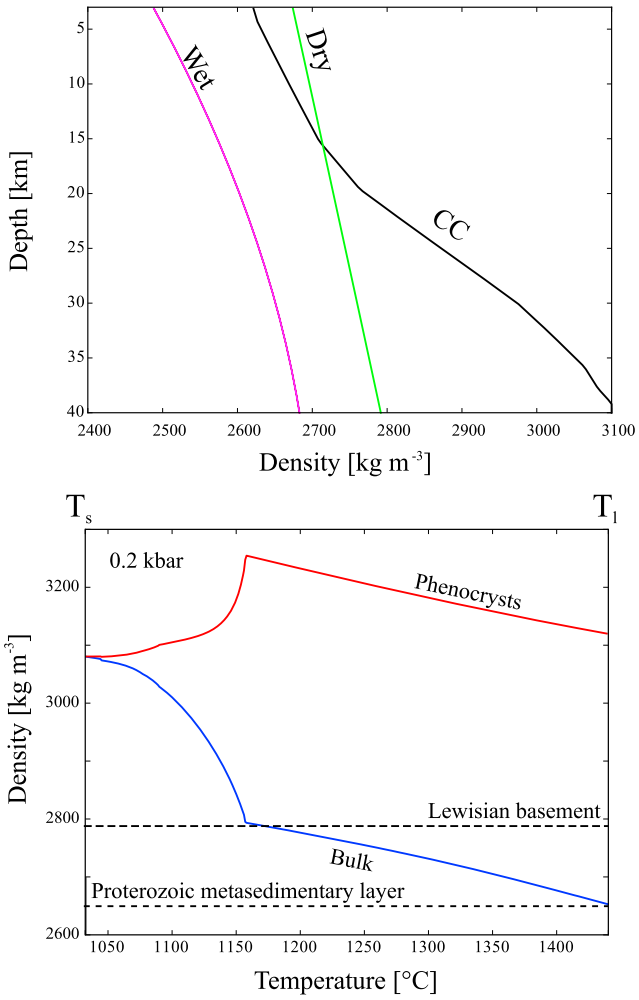


Figure 1. Density of systems calculated with the package MELTS at the FMQ redox buffer. (top) Density of dry primitive basalt (composition is that of residual glass HK#19 [*Hirose and Kushiro*, 1993]) as function of depth compared to the average density model of continental crust (CC) [*Christensen and Mooney*, 1995]. Pink line corresponds to the same composition with 2% water. (bottom) Density of partially crystallized parent basaltic magma for the Rum intrusion, Scotland, between the liquidus and solidus (T_l and T_s, respectively). The blue line shows the bulk density of the whole partially crystallized magma, including residual melt and phenocrysts. The red line corresponds to the bulk density of the solid phases. Parent melt composition is that of M19 groundmass [*Holness et al.*, 2007], and pressure was set at the relevant upper crustal value (0.2 kbar). Densities of the Proterozoic sedimentary cover and the underlying Lewisian gneiss, between which the intrusion was emplaced, are shown as dashed lines [from *Emeleus et al.*, 1996].

Table 1 lists data for several well-known intrusions, including density values for the initial magma and country rock, as well as for the mafic cumulates that characterize the present-day body. In all cases, the initial magma was very close to being neutrally buoyant with respect to encasing rocks, in contrast to the final intrusion that is much denser than them. In the Sept-Iles mafic intrusion, all cumulate rocks have densities that are higher than that of the Grenvillian basement hosting them, including the evolved monzogabbros and mafic syenites of the Upper Series [*Loncarevic et al.*, 1990]. As shown in Table 1, the density contrast between the intrusion and encasing rocks is small and slightly negative (it could be zero given the uncertainties on density values) upon emplacement and is very large and positive in the postcrystallization phase. This very large density increase implies a buoyancy reversal likely to induce a marked change in the deformation regime of encasing rocks.

2.2. The Shapes, Horizontal Outlines, and Aspect Ratios of Mafic Intrusions

Figure 2 shows the horizontal outlines of three mafic complexes of different sizes, the Ardnamurchan, NW Scotland, the Sept-Iles, Quebec, and the Bushveld, South Africa. The first two intrusions are nearly circular with radii of about 3 km and 40 km, respectively. Their remarkably regular outlines are consistent with lateral

Table 1. Densities of Intrusive Mafic Rocks (ρ_i), Encasing Rocks (ρ_c), and Parental Magmas (ρ_m), for a Few Well-Studied Mafic Intrusions[a]

Intrusion	ρ_i (kg m^{-3})	ρ_c (kg m^{-3})	ρ_m (kg m^{-3})	Gravity Anomaly (mGal)	Volume (km^3)	Aspect Ratio
Ardnamurchan				30[b]	2 10^2	1
Rum	3100–3200[c]	2650–2800[c]	2640[d]	75[c]	5.4 10^2	0.5
Sept-Iles	3000–3200[e]	2760–2820[e]	2680[f]	60[e]	2.8 10^4	0.2
Bushveld	3000–3200[g]	2700–2870[g]	2780[h]	60–80[g]	4.0 10^5–1.0 10^6 [i]	0.04

[a] ρ_m has been calculated with MELTS at the liquidus temperature in the appropriate pressure range. Aspect ratio is thickness over radius.
[b] *Burchardt et al.* [2013].
[c] Densities of Proterozoic metasedimentary cover and Lewisian gneiss basement [*Emeleus et al.*, 1996].
[d] Calculated using composition M9 of *Holness et al.* [2007].
[e] *Dion et al.* [1998].
[f] Parental magma composition of *Namur et al.* [2010].
[g] *Cole et al.* [2014].
[h] Parental magma composition of *Yudovskaya et al.* [2015].
[i] *Cawthorn and Walraven* [1998].

extension from a central feeder zone. The larger Bushveld Complex stretches over an ≈65,000 km^2 area and is lobate in outline with four extensions, one of which lies underneath the Karoo volcanics to the south. As convoluted as it may seem, this outline is not highly irregular: it is circumscribed within an ≈400 km wide circle, and its four lobes have similar dimensions and are arranged at almost right angles to one another. This raises the question of what was responsible for such a complex arrangement. The three intrusions are characterized by different aspect ratios (thickness over radius): ≈1.0 for the Ardnamurchan, ≈0.25 for Sept-Iles, and ≈0.04 for the Bushveld. These observations hint at an interesting relationship, such that the aspect ratio decreases as volume increases. These intrusions have all lost parts of their upper igneous sequences due to erosion,

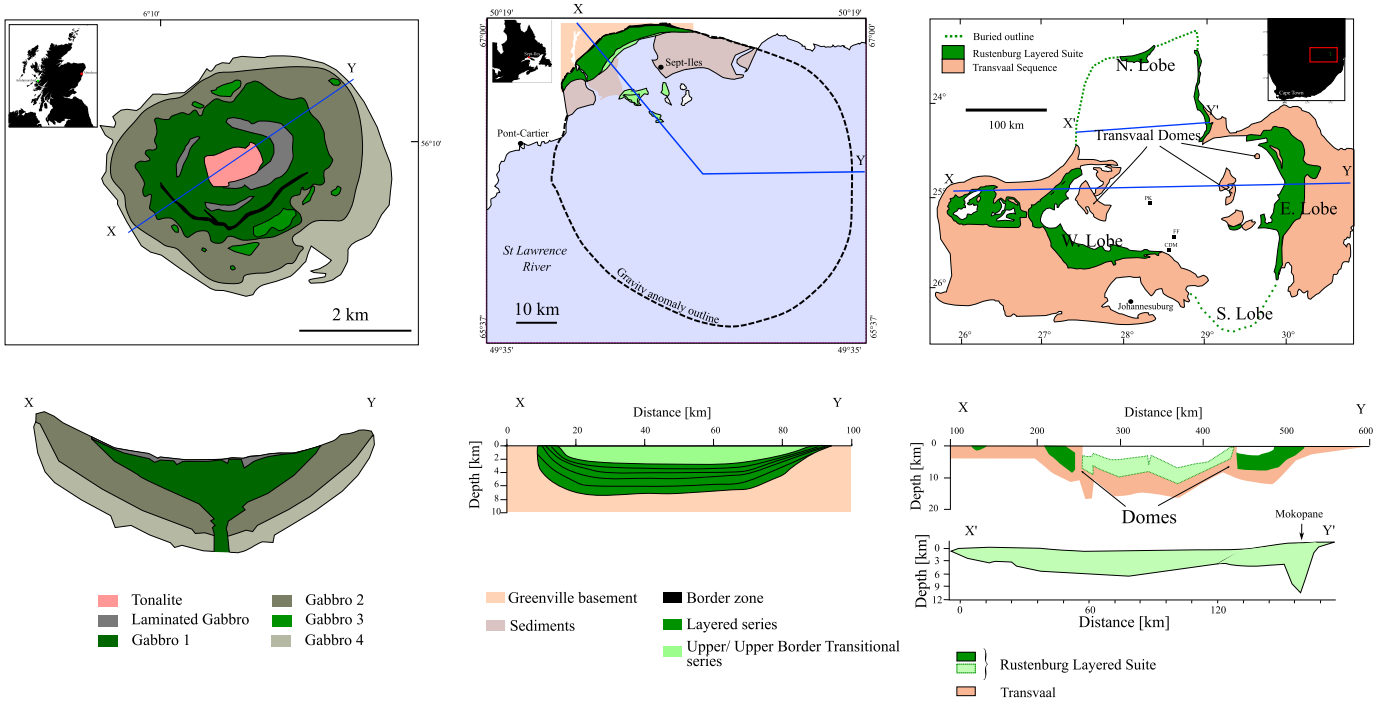


Figure 2. Three mafic intrusions of increasing size. (left) Ardnamurchan, NW Scotland, adapted and modified from *O'Driscoll et al.* [2006]. (middle) Sept-Iles, Quebec, adapted and modified from *Loncarevic et al.* [1990] and *Dion et al.* [1998]. Horizontal outline in the St. Lawrence River from gravity data. (right) Bushveld, South Africa, adapted from *Webb et al.* [2004], *Cole et al.* [2014], and *Cawthorn* [2015]. Cross sections from seismic, magnetic, and gravity data. Note the thick outer ring with a complete igneous sequence (Figure 2, middle) and the deep protrusion into the basement at the eastern end of the *X*′-*Y*′ cross section (Figure 2, bottom). Note also that the basal Lower Zone igneous sequence is missing from the central part of the complex.

Table 2. Flow Laws for Different Crustal Rheologies[a]

Rheology	A (MPa^{-n} s^{-1})	n	Q (kJ mol^{-1})
Wet granite	2×10^{-4}	1.9	140
Quartzite	10^{-4}	2.4	160
Diorite	3.2×10^{-2}	2.4	212

[a]Wet granite is from *Ranalli and Murphy* [1987], quartzite from *Kohlstedt et al.* [1995] and diorite from *Ranalli* [1995].

so that their present-day aspect ratios are slightly smaller than their original ones prior to unroofing. Accounting for this would change the aspect ratios by much less than a factor of 2 and would not modify their ordering. One could add the Rum intrusion, Scotland, to the list [*Emeleus and Troll*, 2014]. The Rum is nearly circular in outline and, with its average radius and thickness of about 7 km and 3.5 km, respectively, has an aspect ratio of ≈0.5, which fits nicely into the same trend. According to a preliminary gravity survey, however, it has an axial root extending to about 15 km depth [*Emeleus and Troll*, 2014], and its shape is not captured accurately by an aspect ratio. It would be desirable to add other mafic intrusions, but several factors prevent this. Many mafic intrusions, including the well-known Great Dyke, Zimbabwe, the Muskox, NW Territories, Canada, and the Jimberlana, Australia, have been fed from long fissures [*Wilson*, 1996; *Irvine*, 1970; *McClay and Campbell*, 1976]. Similarly, the pear-shaped horizontal outline of the Kiglapait intrusion, Labrador, hints at an elongated feeder zone [*Morse*, 2015]. These four intrusions are funnel shaped with pointed axial downward extensions, for which the very notion of aspect ratio is meaningless. The shapes and internal structures of these intrusions are relevant to the physical model of this study, however, and will be discussed at the end of the paper.

2.3. Deformation of Host Rocks

Rock deformation may be achieved by different mechanisms depending on temperature and on the magnitude of deviatoric stresses that are applied. At temperatures that prevail in magmatic environments, one expects ductile behavior described by power law creep:

$$\dot{\epsilon} = A\sigma^n \exp\left(\frac{-Q}{RT}\right) \tag{1}$$

where $\dot{\epsilon}$ is the strain rate, σ is the deviatoric stress, Q is the activation enthalpy, T is temperature, A some constant, and n is the flow law exponent. The heterogeneity and variety of crustal rocks makes it difficult to settle on a single representative flow law, and we have considered three different cases, focusing on the upper and middle crusts (Table 2).

Stresses that are applied to encasing rocks by an intrusion depend on shape and dimensions, but they must be of the order of $\sigma \approx \Delta\rho g h$, where $\Delta\rho$ is the density contrast between the intrusion and host rocks, g is the acceleration of gravity, and h is the intrusion thickness. The density contrast changes with time as magma crystallizes, from small negative or positive initial values between 50 and 100 kg m^{-3} for the incoming melt to positive values in a 300–400 kg m^{-3} range for the final mafic body (Table 1). For intrusion thicknesses in a 5–10 km range, σ is in a range of $3 \times 10^6 - 3 \times 10^7$ Pa. One can define an effective viscosity as $\mu = \sigma/\dot{\epsilon} \sim \sigma^{1-n}$, which is shown as a function of ambient temperature in Figure 3 for $\sigma = 10^7$ Pa. For mature crustal magmatic environments with temperatures in a 500–900°C range, viscosity values are in a range of 10^{15}–10^{20} Pa s, corresponding to strain rates of 10^{-13} s^{-1} or more. Over the lifetime of a magmatic system, which may exceed 1 Myr, such strain rates allow for large deformation of encasing rocks.

2.4. Emplacement and Postemplacement Processes

It is now clear that intrusions grow in piecemeal fashion over long time spans that typically exceed several hundreds of thousand years [*Annen and Sparks*, 2002; *Annen et al.*, 2006; *Glazner et al.*, 2004; *Michaut and Jaupart*, 2006]. Prior to magmatic activity, ambient temperatures are small at shallow to middle crustal depths, implying that early intrusions cool down rapidly and have already solidified to a large extent when the next melt batch comes in. In these conditions, it takes a long time for a sizable (i.e., kilometer-sized) magma reservoir to form. This condition does not depend on thermal constraints only but also on mechanical ones. In cold country rock, as shown by Figure 3, ductile deformation can be ruled out, so that magma intrusion proceeds through hydraulic fracturing involving elastic and brittle deformation, which generates thin and long sills with thicknesses of a few meters to a few tens of meters [*Sisson et al.*, 1996; *Michaut*, 2011]. Thus, a large number

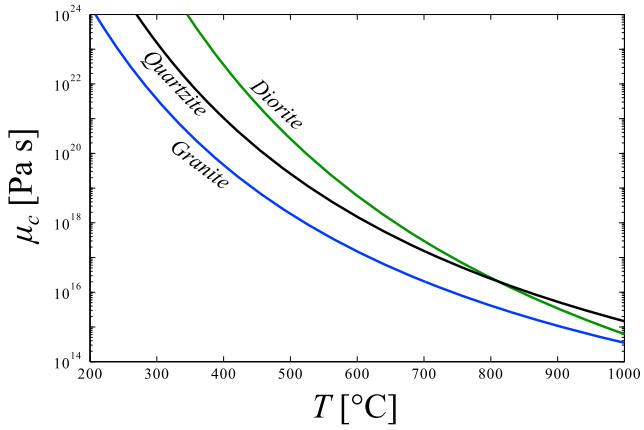


Figure 3. Calculated effective viscosities for a characteristic deviatoric stress of 10 MPa as a function of temperature. Flow laws and references are given in Table 2.

of individual injection events are needed to build a kilometer-sized body. With time, repeated magma inputs raise temperatures in host rocks with two consequences. One is that a long-lived magma reservoir may exist, such that a sizable amount of melt survives through quiescence intervals. Another consequence is that host rocks can deform in a ductile regime. Ductile deformation may be significant both during and after an injection event. During injection, it prevents the buildup of large stresses at the reservoir walls and rupture leading to eruption, which allows reservoir growth [*Jellinek and DePaolo*, 2003; *Del Negro et al.*, 2009]. In mature magmatic provinces, near-surface geothermal gradients are elevated [*Springer and Förster*, 1998; *Blackwell et al.*, 1990; *Manga et al.*, 2012], indicating that temperatures of 400–500°C are reached at depths of 7 to 10 km and also that magmatic activity has been maintained for a time that is sufficiently long for heat to propagate to the surface. In time τ, heat diffusion proceeds over distance $\delta \approx 2\sqrt{\kappa\tau}$, where κ is thermal diffusivity, which is about 10 km for $\tau = 1$ Myr and $\kappa = 10^{-6}$ m^2 s^{-1}. This shows that a large crustal volume gets heated in the lifetime of a magmatic system. Evidence for ductile deformation in such systems is provided by geodetic data [*Newman et al.*, 2001; *Masterlark et al.*, 2010].

One may thus expect different situations in early and late phases of magmatism. Early phases are characterized by the buildup of a magma reservoir with dimensions that are determined by hydraulic fracturing and brittle-elastic deformation. Later phases, in contrast, see sizable magma reservoirs embedded in heated rocks that deform in a ductile regime. In this paper, we focus on the latter and consider the behavior of a magma body of fixed volume once the input of new magma has dwindled to negligible amounts, in what we call postemplacement processes. We evaluate quantitatively the separation between emplacement and postemplacement processes at the end of the paper. Two different postemplacement processes must be considered because of the density change that occurs due to cooling and crystallization. An intrusion filled with magma that is still buoyant will spread laterally at its emplacement level. As its density increases and eventually exceeds those of encasing rocks, as explained above, it will begin to sag and to founder. We shall show that foundering proceeds in different regimes depending on the aspect ratio of the intrusion, which increases past its emplacement-controlled value if spreading occurs. For this reason, we allow for a full postemplacement sequence involving both spreading and foundering. In geological reality, spreading may be limited and may not affect the intrusion dimensions significantly, a possibility that will be assessed quantitatively using our results.

3. Laboratory Experiments

3.1. Experimental Setup and Working Fluids

Investigating in the laboratory the behavior of an intrusion that spreads at a density interface, loses heat to colder surroundings, and undergoes a buoyancy reversal requires very fine tuning of the densities involved. We have arranged for the compositions of the three fluids to be such that the density of the intrusion at its starting temperature is initially between those of the two encasing layers, i.e., larger than the upper one and smaller than the lower one, and increases to a value above that of the lower layer as it cools down.

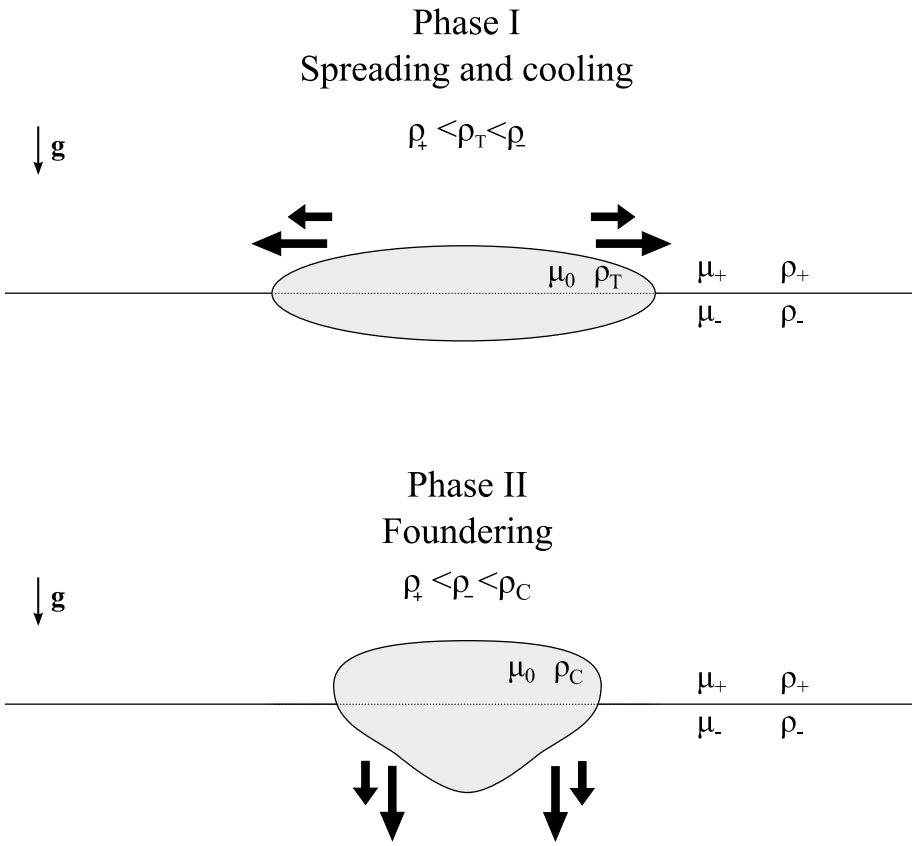


Figure 4. Schematic sketch of the two postemplacement processes that are studied in our laboratory experiments. (top) At the beginning, the intrusion is hot, has an intermediate density between the two ambient fluids, and spreads at the interface. (bottom) In a second phase, the intrusion has cooled down and becomes unstable due to its negative buoyancy.

Cooling induces a buoyancy reversal mimicking that which is induced by crystallization in basaltic melts. With the relatively small temperature range that can be achieved in controlled conditions (a few tens of degrees) and the very small density change due to temperature that results, density differences between the working fluids had to be very small (less than 1%), which made for very tricky experiments. These delicate requirements meant that we had to prepare our own working fluids so that we could vary their properties at will. Details about experimental methods can be found in the appendix. The viscosity of the intrusion was about equal to, or less than, that of the encasing fluids, which is appropriate for melt and partially crystallized magma in colder country rock.

Typically, the room and host fluids were at a temperature of 25°C and intruding fluids were prepared at temperatures around 45°C. The density reversal was set to occur at about 30°C. Due to the very tight constraints on density, it was easier to change viscosity values and the volume of intruding fluid than to play with buoyancy in order to generate different deformation regimes. Nevertheless, the experiments spanned a sufficiently wide range of dimensionless parameters (to be defined later) for a useful analysis. Definitions and symbols for the various variables are given in Figure 4, whereas the fluid properties and parameters that characterize the experiments are listed in Table 3.

With all the preparations and measurements of physical properties that were required, each experiment took about a week. We report on 12 experiments which followed the same protocol. In a tank filled with two different liquids, a fixed volume of hot fluid was injected through a small nozzle right at the interface between the two fluids in the shortest amount of time possible (in a 5–20 s range). The intrusions spread to a maximum radial distance of 7–8 cm, and we made sure that the tank was sufficiently large (40 × 40 × 40 cm) to minimize the influence of the side walls and depths of the encasing fluids. This requirement meant that we had to deal with very large fluid volumes. We measured the intrusion radius from photographs taken from both the side

Table 3. Table of the Experimental Parameters (Definitions Given in Figure 4)[a]

Run	ρ_-	ρ_+	ρ_i	μ_-	μ_+	μ_i	V	W	B	Instability[b]	λ_m^*/R_c	λ/R_c	α_c
1207	1010	1002	1013	10.0	10.0	10^{-2}	135	10^{-3}	3.6	Td			0.78
1209	1010	1002	1012	10.0	10.0	10^{-2}	102	10^{-3}	5.0	Td			0.5
1221	1010	1002	1013	1.0	1.0	10^{-2}	85	10^{-2}	3.5	Jf	1.8	0.3	0.13
1406	1013	1000	1016	5.4	4.1	2.2	50	0.46	5.3	Jf	0.98	0.6	0.17
1408	1014	1000	1017	5.2	4.5	2.2	102	0.45	5.6	Jf	0.92	0.2	0.16
1411	1013	1000	1016	6.0	6.5	0.6	25	0.10	5.3	Td			0.42
1412	1014	1000	1017	5.1	4.9	2×10^{-3}	53	4×10^{-4}	5.6	An	7.0		0.18
1413	1015	1000	1017	5.4	5.2	2×10^{-3}	104	3.7×10^{-4}	8.5	An	10.2		0.26
1414	1014	1000	1018	5.4	4.4	2×10^{-3}	39	4×10^{-4}	4.5	An	7.8		0.24
1425	1014	1000	1018	4.8	5.1	5.1	28	1.03	4.5	Jf	1.42	0.5	0.24
1426	1012	1000	1017	4.8	5.1	5.1	55	1.03	3.4	Jf	1.58	0.5	0.25
1427	1014	1000	1017	4.8	5.1	5.1	157	1.03	5.6	Jf	1.5	0.3	0.26

[a]Densities (ρ) at room temperature are given in kg m^{-3}, viscosity (μ) in Pa s, and volume (V) in cm^3. $W = \mu_i/\mu_- \approx \mu_i/\mu_+$ and $B = (\rho_i - \rho_+)/(\rho_i - \rho_-)$ are the viscosity ratio and the buoyancy number, respectively. λ_m* is the optimal wavelength of the Rayleigh-Taylor instability for the W and B values, following *Lister and Kerr* [1989a] (see text for explanations). λ is the wavelength of the "jellyfish" pattern. Both wavelengths have been scaled to the unstable disk radius R_c. α_c is the intrusion aspect ratio at the onset of foundering (see text for explanations).
[b]The instability pattern is labeled as follows: Td for teardrop, Jf for jellyfish, and An for annular.

and the top after careful calibration with a grid that had been immersed in the fluids. The intrusion thickness was determined from the color spectrum of the photographs using Beer-Lambert's law (the procedure was tested on layers of known thicknesses). We verified that the reconstructed intrusion volume was identical to the injected one.

The experiments involve different intrusion volumes and encasing fluid viscosities (Figure 4) and lead to instabilities with different characteristics and dimensions. For the spreading phase, we follow the theoretical analysis by *Lister and Kerr* [1989a] and show experimental results with dimensions scaled to $V^{1/3}$ and time scaled to $(\mu_- + \mu_+)/(2\rho_T g' V^{1/3})$, where V is the intrusion volume, μ_+, μ_-, ρ_+, and ρ_- are the viscosities and densities of the upper and lower fluids, and ρ_T is the initial density of the intruding fluid (Figure 4). g' is the "reduced" gravity such that

$$g' = \frac{(\rho_- - \rho_T)(\rho_T - \rho_+)}{\rho_T(\rho_- - \rho_+)} g \tag{2}$$

For later use and for simplicity, we define an effective density contrast $\Delta\rho_T$ as follows:

$$\rho_T g' = \frac{(\rho_- - \rho_T)(\rho_T - \rho_+)}{\rho_- - \rho_+} g = \Delta\rho_T g\,. \tag{3}$$

We use different scales for the foundering process, as explained in the relevant sections.

3.2. Three Postemplacement Phases

We use one particular experiment to describe the behavior of an intrusion (experiment #1209, Table 3 and Figure 5). We track the evolution of the intrusion using measurements of the radius and of the depth of its center of mass, which was determined from the barycenter of photograph pixels. The shape of the intrusion and its changes are shown in Figure 5.

In the initial "spreading" phase, the intrusion behaves as a viscous gravity current. Its radius increases steadily, and its center of mass goes down. The end of this phase is such that the intrusion radius reaches a maximum and starts to decrease (Figure 5). The second phase is one of sagging, with parts of the intrusion that have become denser than the underlying liquid. The intrusion radius decreases, and the center of mass continues to go down. This phase leads to a final one, such that the increasingly dense intrusion begins to sink wholesale. The onset of this third phase is characterized by an accelerating downward motion of the center of mass. In Figure 5, the intrusion behaves as a pendant teardrop that gets stretched over the vertical. At later times, a narrow neck forms that separates a funnel-shaped upper part from an ovoid-shaped lower part.

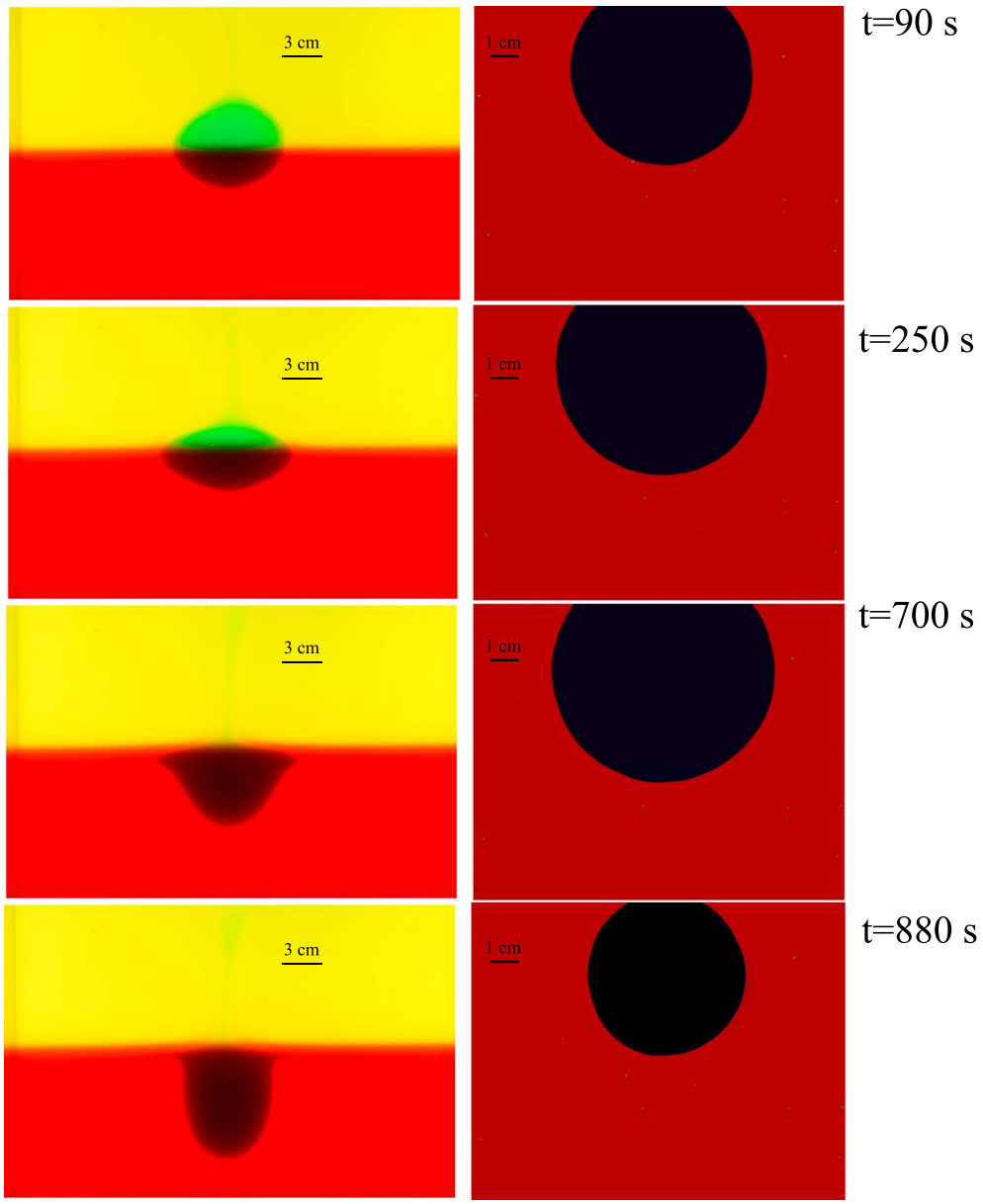


Figure 5. Snapshots of experiment 1209, (left column) side view and (right column) view from above. Note that the intrusion radius first increases and decreases as a drop begins to form.

All our experiments lead to the sinking of the intrusion, which eventually ends up at the base of the tank. This is due to the behavior of the encasing fluids, which are strictly Newtonian and which cannot support stresses statically. In geological reality, rocks have a finite strength and we expect that the instability does not go to completion and that all or part of the intrusion remains at the initial emplacement level. This was shown to be the case using numerical calculations that allow for brittle, elastic, and ductile deformation and that are described elsewhere [*Roman and Jaupart*, 2016]. These calculations were carried out in two space dimensions due to the very large number of grid points that were needed to track deformation accurately and complement the present experiments, which illustrate three-dimensional patterns.

A few important results are worth emphasizing. Intrusion dimensions may not be determined at the emplacement stage and may be acquired at a later time. The final intrusion shape may bear little relationship to the initial one. Buoyancy reversal induces a change of stress regime in roof rocks, from extension in the spreading phase to compression in the sagging and foundering phases. These states of stress are due to the density distribution and do not depend on the deformation regime.

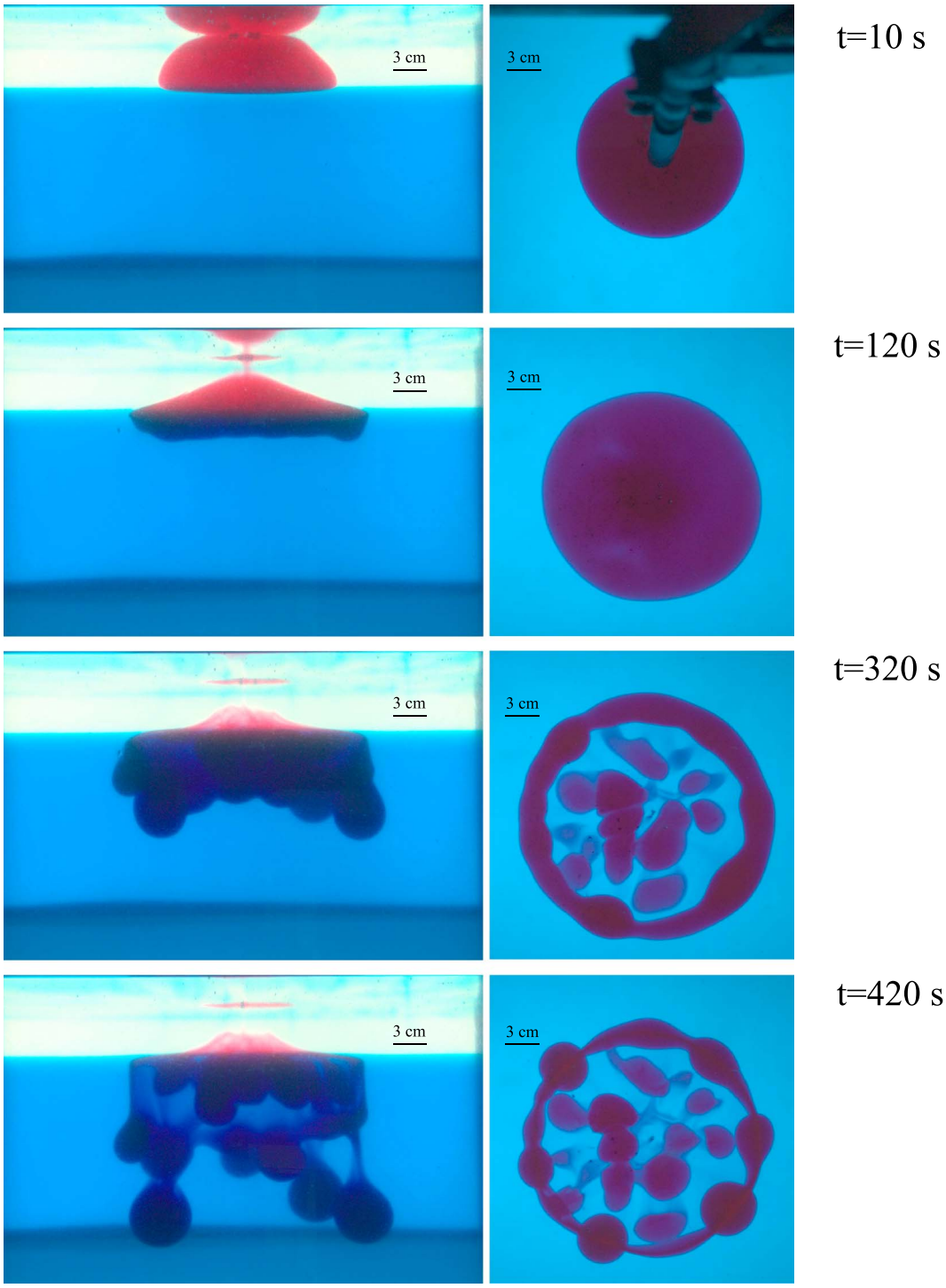


Figure 6. Snapshots of experiment 1427, which show the development of the jellyfish instability. Note that the outer ring becomes unstable in the form of several downwellings that disrupt the smooth planform of the intrusion.

3.3. Three Different Types of Instability

We observed three different types of instability which we illustrate by three particular experiments. The first type of instability, called "teardrop," has just been described (Figure 5). The other two types develop in intrusions that have spread to large horizontal distances, such that their aspect ratios (thickness over radius) are small. One should note that, in all cases, the spreading phase is such that the intrusion is thickest at its center, implying that a basin or bowl shape may not necessarily indicate active sagging of the floor.

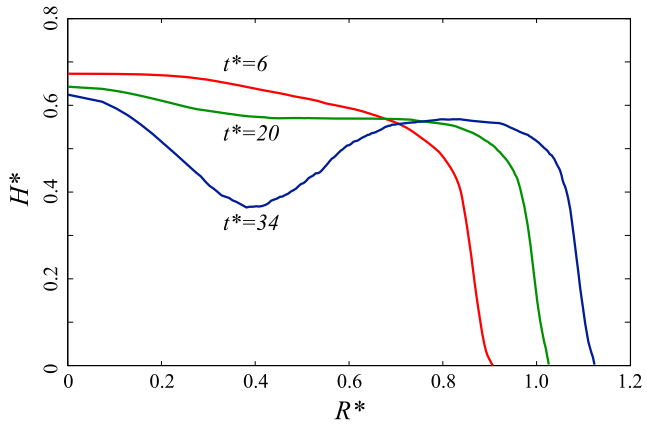


Figure 7. Radial variation of dimensionless intrusion thickness for experiment no. 1426, which became unstable in the jellyfish regime. Profiles are shown at three different dimensionless times: before the onset of instability (red), at the onset of instability (green), and once the thick outer ring is well developed (blue).

One instability was dubbed jellyfish, due to its peculiar lumpy interior circumscribed by a thick outer ring (Figure 6). To understand how this peculiar pattern comes about, we follow how the intrusion thickness evolves with time. In the early spreading phase, the intrusion thins as it propagates laterally and there is no detectable sagging. At the onset of instability, a thick outer ring develops at the edge of the intrusion (Figure 7) and begins to founder in an initially almost uniform curtain-like annular downwelling (Figure 6). The instability is initiated at the outer edge because it is there that the intrusion is coldest and densest. It acts to drain fluid from the central part of the intrusion, which thins and becomes unstable in a network of downwellings and upwellings. The annular edge downwelling is also unstable and splits into a set of evenly spaced drops. This generates a wavy and irregular horizontal planform with "lobes" that protrude laterally into the surrounding fluid. Figure 8 illustrates the downwellings that develop at the edge of intrusions with different volumes and shows that their dimensions approximately scale with $V^{1/3}$.

The third type of instability is an extreme form of the jellyfish one and will be called "annular" (Figure 9). It follows the same initial development with an outer ring that becomes unstable and drips down. In this case, however, the ring becomes thicker than in the jellyfish case and rapidly drains fluid from the central region, thereby preventing the generation of downwellings there. The annular edge downwelling also becomes unstable but in a more irregular pattern than previously, resulting in a marked lobate planform (Figure 9). We attribute this to the wavelength of the instability which is not small compared to the ring circumference and cannot manifest itself in an evenly spaced pattern. This peculiar instability regime was observed in three independent experiments involving different volumes.

4. The End of the Spreading Phase

The intrusion initially spreads as a viscous gravity current, which has been studied using both theory and laboratory experiments. The main variables are shown in Figure 4. Flow is driven by buoyancy and resisted by shear at the top and bottom as well as stresses at the tip [*Lister and Kerr*, 1989a; *Koch and Koch*, 1995]. As the intrusion thins and its aspect ratio decreases, shear stresses at the top and bottom become increasingly important and rapidly dominate the momentum balance. The flow radius and thickness tend toward the lubrication solution of *Lister and Kerr* [1989a]:

$$R(t) \sim \left(\frac{\rho_T g' V^2}{\mu_+ + \mu_-}\right)^{1/5} t^{1/5}$$
$$h(t) \sim \left(\frac{(\mu_- + \mu_+)V^{1/2}}{\rho_T g'}\right)^{2/5} t^{-2/5} \quad (4)$$

where the variables have already been defined above. Vertical gradients of the horizontal velocity are necessarily small in a thin current, implying that the intrusion viscosity does not appear. An important point is that these scaling laws describe an asymptotic behavior independent of the initial shape of the intrusion

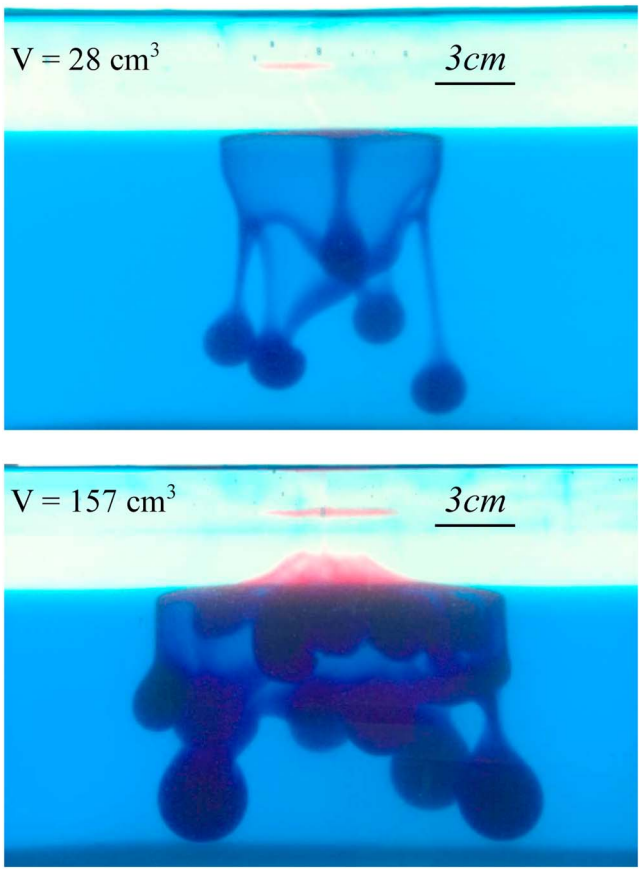


Figure 8. The development of downwellings at the leading edge of the intrusion in two different experiments (nos. 1425 and 1427) in the jellyfish regime. The only difference between these two experiments is the intrusion volume, which varies by a factor of 5.6. All the other parameters are identical. This shows that the downwelling dimensions increase with the intrusion volume.

when it begins to spread. How the intrusion was built is therefore irrelevant, an important point for geological applications.

The intrusion starts to spread at its injection temperature, with density noted ρ_T. As it cools down, its density increases such that it eventually becomes denser than the surrounding fluids, which signals the end of the spreading phase. We use a simple analysis to determine the critical aspect ratio of the intrusion when it begins to founder. We are not interested in the onset time of the sagging/foundering process, which depends on how fast it develops, but in the aspect ratio of the intrusion at that time. We note that the intrusion thickness decreases with time, while the thickness of cooled intrusion material increases. Cooling is achieved by diffusion over a thickness that scales as $\delta = \sqrt{\kappa t}$, where κ is thermal diffusivity, and affects the whole flow when $h \sim \delta$. Due to the power law exponents involved for $h(t)$ and $\delta(t)$, diffusion proceeds faster than the intrusion can thin when this condition is met and the intrusion dimensions can only change slowly until foundering develops in earnest. We thus argue that the critical value of the aspect ratio must be very close to that when the condition that $h \sim \delta$ is met. Substituting this condition into equation (4), the critical time for unstable conditions is

$$t_c \sim \left(\frac{(\mu_- + \mu_+)V^{1/2}}{\rho_T g' \kappa^{5/4}} \right)^{4/9} \tag{5}$$

At this time, the intrusion thickness and radius are H_c and R_c, respectively, corresponding to a critical aspect ratio:

$$\alpha_c \sim \frac{H_c}{R_c} \sim \left(\frac{(\mu_- + \mu_+)\kappa}{\rho_T g' V} \right)^{1/3} = Ai^{-1/3} \tag{6}$$

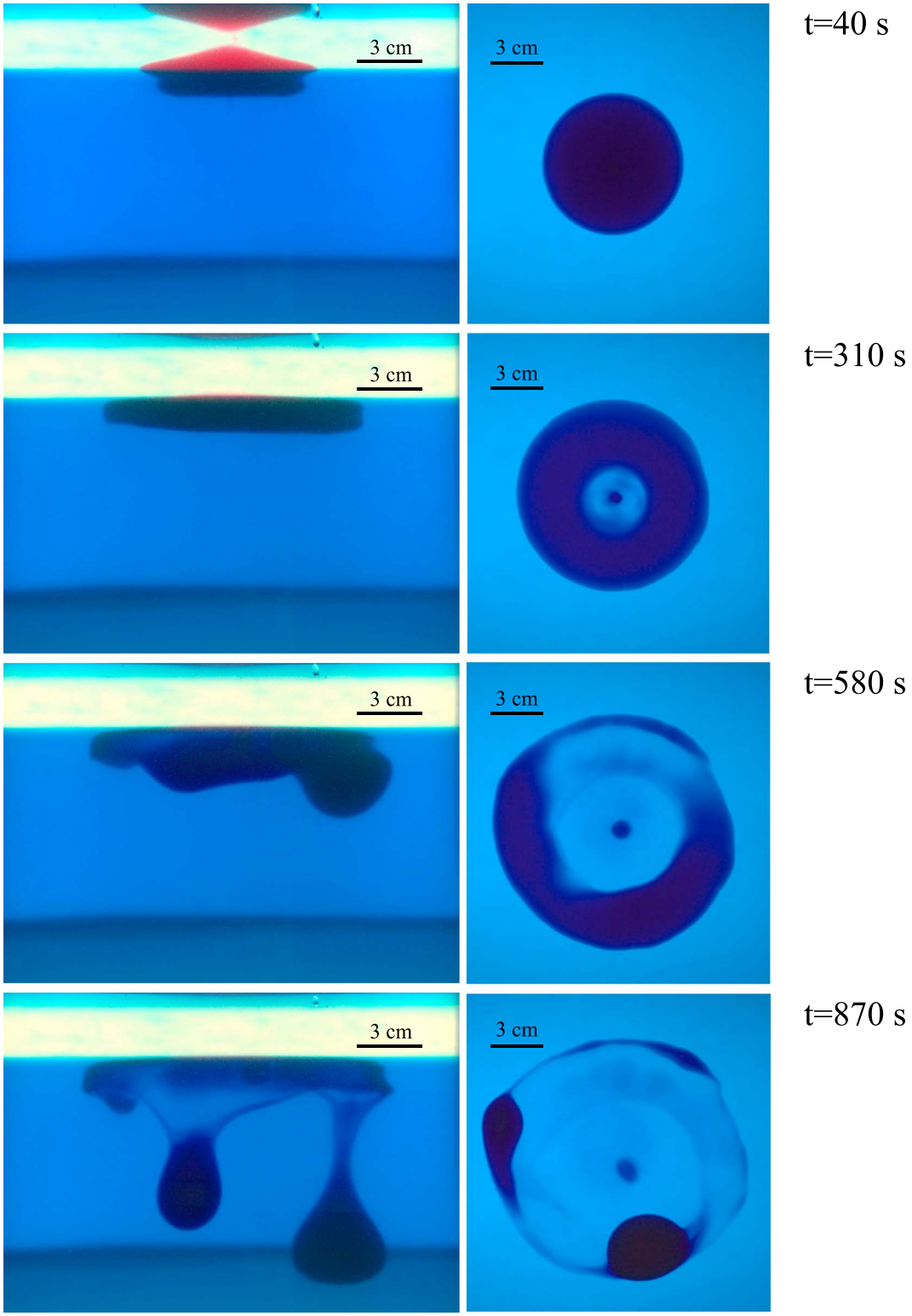


Figure 9. Snapshots of experiment 1413 showing the development of the annular instability. Note the marked thinning of the central region at $t = 310$ s.

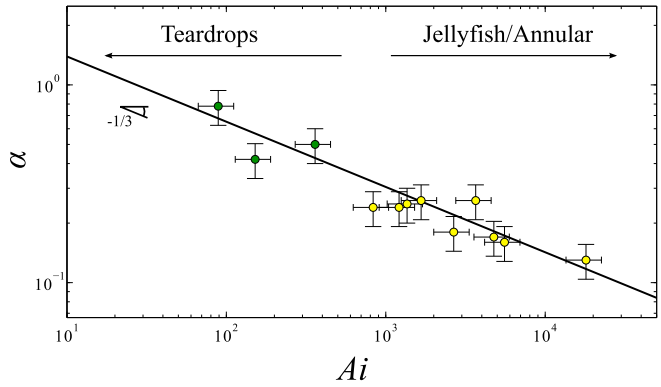


Figure 10. Aspect ratio of the intrusion at the end of the spreading phase as a function of dimensionless number $Ai = \frac{\rho_T g' V}{\kappa \mu}$. The best fit relationship with $\alpha_c \sim Ai^{-1/3}$, as predicted by dimensional analysis, is shown as a black solid line. Experiments developing teardrop instabilities are shown in green, while experiments developing in either the annular or the jellyfish instabilities are shown in yellow. The transition between the two regimes is seen to occur at $\alpha_c \approx 0.4$ and $Ai \approx 500$.

where dimensionless number Ai is

$$Ai = \frac{\rho_T g' V}{(\mu_- + \mu_+)\kappa}. \tag{7}$$

Ai takes the form of a Rayleigh number and is discussed below.

The predictions of equation (6) are consistent with the experimental data (Figure 10). In principle, the above solutions for viscous spreading are only valid for thin currents with small aspect ratios, but they seem to account for intrusions with aspect ratios in a 0.4–0.8 range quite well. Data at small aspect ratios are too tightly clustered to allow an independent test, unfortunately, but they are certainly consistent with the proposed relationship. A best fit analysis with the exponent fixed at the predicted value of $-1/3$ yields the following relationship:

$$\alpha_c = (2.8 \pm 0.10) Ai^{-1/3}. \tag{8}$$

All else being equal, the larger the volume, the smaller the aspect ratio should be. We have described in section 1 several mafic intrusions that do conform to these systematics, but one should be wary of pushing this too far: continental crust thickness is constrained to be in a rather restricted range of about 30–70 km, which does not allow for arbitrarily thick bodies.

The dimensionless number Ai can be interpreted by analogy with the Rayleigh number that characterizes thermal convection. It may be expressed as the ratio between two velocity scales, one for spreading and the other for heat diffusion. The latter is simply

$$U_d = \frac{\kappa}{H} \tag{9}$$

where H is a characteristic thickness. The spreading rate scale is derived from the bulk horizontal momentum balance:

$$\left(\rho_T g' H\right) HR \sim \left[(\mu_- + \mu_+)\frac{U_s}{R}\right] R^2 \tag{10}$$

where R is the radius scale and U_s is a characteristic velocity. This equation states that the flow is driven by buoyancy and resisted by viscous shear stress at the upper and lower surfaces. For flow of radius R, the kinematic boundary layer extends to a distance $\sim R$, so that the typical strain rate is U_s/R. This balance leads to the scaling laws of *Lister and Kerr* [1989a] that have been used above. A scale for the spreading rate is thus

$$U_s \sim \frac{\rho_T g' H^2}{\mu_- + \mu_+} \tag{11}$$

To describe the bulk flow behavior, we set $H \sim V^{1/3}$ and $R \sim V^{1/3}$ and find that

$$\frac{U_s}{U_d} = \frac{\rho_T g' V}{(\mu_- + \mu_+)\kappa} = Ai \tag{12}$$

Thus, the larger *Ai* is, the faster spreading is compared to heat diffusion, which allows the flow to reach increasingly large distances before buoyancy reversal. For *Ai* values that are smaller than some threshold, spreading is not sufficiently rapid for the intrusion to extend past its starting position and is effectively suppressed. A rough estimate for this threshold value is 50. This may seem large, but one may be reminded that the critical value of the Rayleigh number for the onset of thermal convection is typically 10^3.

5. The Three Instability Regimes

5.1. Three Dimensionless Numbers

Once the intrusion has become denser than its host due to cooling, the dynamics change drastically. The temperature distribution is not uniform, but we characterize all densities at the initial background temperature (in the "cold" limit) for simplicity. The intrusion density is now ρ_i instead of ρ_T. The change is small in absolute value but large in terms of buoyancy, which has changed sign. The intruding fluid viscosity is μ_i, and in our experiments, the two encasing fluids have almost the same viscosity. Three dimensionless numbers characterize the intrusion behavior. One is the aspect ratio $\alpha_c = H_c/R_c$, and the other two are the viscosity and buoyancy ratios $W = \mu_i/\mu_- = \mu_i/\mu_+$ and $B = (\rho_i - \rho_+)/(\rho_i - \rho_-)$, respectively. The buoyancy ratio does not vary much in geological conditions. It must be larger than 1 because $\rho_+ < \rho_-$ (this is required for a stable crustal stratification and is achieved in all the experiments) and may be as high as 5 for a low-density sedimentary cover and a high-density gneissic basement. We have not investigated a very large range for this reason and do not expect that the *B* value affects the results significantly. This was indeed found to be the case (Table 3).

We find that the aspect ratio dictates the form of the instability that develops. It takes aspect ratios larger than about 0.4 for the teardrop regime to occur, independently of the viscosity ratio, and smaller values for the other two regimes (Table 3 and Figure 10). The jellyfish and annular regimes seem to be mostly sensitive to the viscosity ratio, with $W > \approx 10^{-3}$ for the former and $W <\approx 10^{-3}$ for the latter, independently of the aspect ratio (with the proviso that it must be less than about 0.4).

5.2. The Jellyfish and Annular Instabilities

We briefly discuss some of the guiding principles behind the jellyfish and annular regimes. For analysis, we refer to the Rayleigh-Taylor (RT) configuration of a dense horizontal layer sandwiched between two buoyant ones and use the equations of *Lister and Kerr* [1989b]. We scale dimensions to the dense layer thickness *h*, time to $\mu_i/\Delta\rho g h$, and instability growth rates to $\Delta\rho g h/\mu_i$. Note that the latter two are both written as a function of the intrusion viscosity. Figure 11 shows that the RT instability is weakly sensitive to buoyancy number *B* and is mostly controlled by the viscosity contrast in the parameter domain of our experiments. This is consistent with our observations (Table 3). In the experiments, the intrusion viscosity was equal to or less than those of the two host fluids, leading to *W* values that are equal to 1 or less. This may not be the case in nature if the dense cumulates are fully solidified, such that their rheology would be determined by olivine and pyroxene minerals and could be stronger than the hosts. *W* values would then be larger than 1. Cumulates are hotter than their hosts and may not be fully solidified until late in the cooling sequence, however, in which case their rheology would be affected even by small amounts of interstitial melt. We have allowed for *W* values larger than 1, and they do not modify significantly the results (Figure 11).

The present experimental conditions differ from RT ones in three ways: the dense layer is not isothermal nor are its top and bottom perfectly horizontal, it does not extend to infinity, and it is actively thinning as it gets drained by peripheral downwellings. We ignore the first effect for simplicity and discuss the other two. In a layer extending to infinity and in the absence of surface tension, all perturbations of the two fluid interfaces get amplified. The growth rate depends on two competing processes. One is the formation of a downwelling, with a velocity that is set by a balance between buoyancy and viscous forces in the encasing fluid and that increases with wavelength. The other process is flow within the dense layer that feeds the downwellings, with a velocity that decreases with increasing wavelength. The growth rate reaches a maximum for a critical wavelength $\lambda_m = \lambda_m^* h$, where λ_m^* is a dimensionless wavelength that depends on the two dimensionless numbers *W* and *B*. This result is valid for a layer of finite width only if it is large enough to host several downwellings. For a horizontal disk of diameter $D = 2R$, this condition can be expressed as $\lambda_m <\approx 2R$, which can be rewritten as $\lambda_m/R > \approx 2$ the most unstable wavelength is smaller than the optimal one and scales with *D* and is associated with a smaller growth rate. Another factor is that the unstable layer continuously thins as time progresses because it gets drained by the edge downwelling. The growth rate of the RT instability is an increasing

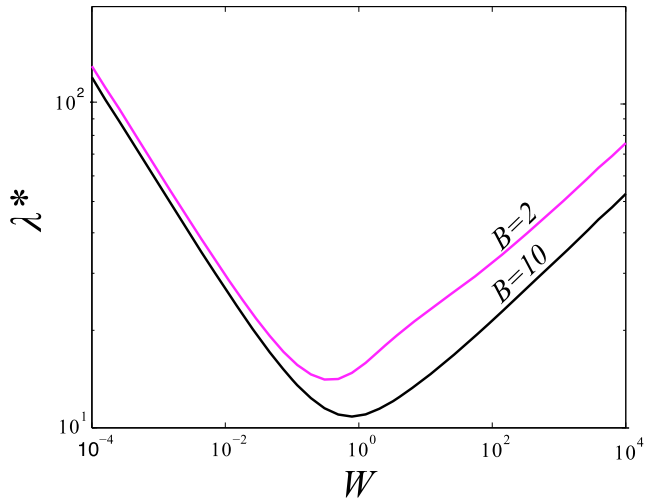


Figure 11. Fastest-growing dimensionless wavelength of Rayleigh-Taylor instability of a dense layer sandwiched between two buoyant ones as function of viscosity contrast W, from the equations of *Lister and Kerr* [1989b]. Violet solid line: $B = 2$, black solid line $B = 10$. The asymptotic relation $\lambda_m^* \propto W^{-1/3}$ predicted by *Lister and Kerr* [1989a] is recovered for viscosity contrasts smaller than 10^{-1}. These results emphasize that within the parameter space of the experiments as well as of natural conditions, results are not sensitive to B.

function of the layer thickness and hence decreases with time in the experiments. For the instability to develop, its growth rate must be larger than the rate at which the disk is being thinned.

In order to evaluate which factor is relevant to our experiments, we compare the observed wavelengths to the theoretical optimal one (Table 3). Observed values are calculated as the average spacing between downwellings in the jellyfish regime. All wavelengths are scaled to the disk radius (i.e., shown as λ/R) as discussed above. Note that these scalings correspond to the layer thickness at the end of the spreading phase, which is the maximum thickness for any given experiment. We find that λ_m/R is about 1 for the jellyfish experiments and greater than 7 for the annular ones. This shows that a dimensionless wavelength near the optimal one can be "activated" in the jellyfish experiments, indicating that the unstable disk radius is not a limiting factor. The observed values of the wavelength are smaller than the theoretical ones, showing that the instability develops when the layer has been thinned significantly. Increasing the viscosity of the surrounding fluids (i.e., decreasing viscosity ratio W) acts to decrease the dimensionless instability growth rate. In this case, which corresponds to the annular experiments, the instability growth rate is much smaller than in the jellyfish experiments, which is not favorable to instability. We conclude that the limiting factor is the competition between the growth of the instability and the thinning of the unstable layer.

The conditions that dictate the jellyfish and annular regimes have not been determined precisely and would deserve a longer investigation. For geological purposes, however, this is not a crucial issue. The jellyfish and annular patterns are very different and can be distinguished from one another with appropriate field observations.

5.3. Transition Between the Teardrop and Jellyfish/Annular Regimes

The most important transition is between the teardrop and jellyfish/annular regimes because they lead to completely different intrusion shapes, with thick and thin axial regions, respectively. According to our experiments, this transition occurs at an aspect ratio of about 0.4, independently of the viscosity ratio. The same change of behavior was observed in 2-D numerical simulations with brittle-elastic-ductile rheology [*Roman and Jaupart*, 2016], albeit at a slightly smaller aspect ratio. From the results of Figure 10 and equation (8), this transition occurs for $Ai \approx 500$.

6. Return to Mafic Intrusions

6.1. Discussion

The basic assumption behind this work is that one can study the behavior of basaltic intrusions using viscous fluids. This is consistent with the analysis of *Jellinek and DePaolo* [2003], who have argued convincingly that

the growth of large magma reservoirs requires viscous relaxation in encasing rocks. The experimental conditions of this study are undoubtedly much simpler than those prevailing in real intrusions. In particular, they gloss over crystallization processes that lead to a wide range of igneous layering structures. Given the large uncertainties in the rheology of crustal rocks and in the background temperature field prior to intrusion, however, definitive answers can only come from local field studies. The ambition of this paper is not to provide such answers but to draw attention to the likelihood of large magma reservoirs going unstable as well as to the various forms that the instability can take. The relevance of our results can be established by evaluating the viscosity values that are required and by comparing predicted intrusion shapes to observed ones, which is done in two separate sections below. Late deformation occurring after the generation of thick ultramafic or mafic cumulates perturbs the layering arrangement in a predictable manner, providing confirmation for the process. This important topic is outside the scope of this paper but deserves a few comments that are given below.

As explained in sections 1 and 2.4, the growth of large magma bodies is a slow and intermittent process, and yet we have made experiments with a fixed intrusion volume. A key point is that it takes a minimum amount of magma for spreading to be significant. This issue can be addressed using equation (11) for the spreading rate, which increases with intrusion thickness and with decreasing viscosity of the host rocks. For spreading to be significant, it must be faster than the intrusion growth rate. For a midsized intrusion like the Rum, Scotland, $H \approx 4$ km [*Emeleus and Troll*, 2014] and, assuming that it got assembled in a 0.1 to 1.0 Myr range, the average reservoir growth rate is in a range of $\approx 10^{-9} - 10^{-10}$ m s^{-1}. Using an average value for $\Delta\rho_T$ of $\approx$ 50 kg m^{-3}, we find that spreading is faster than reservoir growth when the effective viscosity of encasing rocks drops below about 10^{19} Pa s, which can be converted to temperature using Figure 3. This argument can also be turned around as follows. For a given viscosity value, say 10^{19} Pa s, spreading becomes important when the magma body reaches a minimum thickness of about 4 km, corresponding to a full-fledged intrusion.

Two factors simultaneously act to enhance spreading as time progresses: the intrusion grows and encasing rocks weaken as they heat up, implying that spreading will be most active toward the end of the emplacement phase. It will continue once magma supply has stopped and can be described by the asymptotic scaling laws detailed above, which do not depend on initial conditions. Thermal limitations are critical in the upper crust where the intrusions of Table 1 were emplaced because of the small background temperatures that prevailed before the start of magmatic activity. The necessary conditions for spreading and foundering are unlikely to be achieved for small intrusions because of both their small volume and reduced thermal impact on encasing rocks. A case at hand is probably the Ardnamurchan intrusion, with its aspect ratio of about 1 (Table 1). Thermal limitations are less severe in lower crustal environments at high temperature, and it may well be that spreading proceeds faster than intrusion growth even for small magma volumes. As discussed by *Roman and Jaupart* [2016], foundering is likely to be very effective in this case, which may not allow the preservation of large mafic residual bodies. We derive below the viscosity values that are required to account for the intrusion dimensions that are observed.

Some of our conclusions apply even if spreading is not efficient, due, for example, to strong host rocks. In this case, foundering may still proceed due to the large density difference that is induced by crystallization. One may further consider that a layer of dense cumulates may become unstable before the bulk intrusion. For an actively growing cumulate pile, the instability growth rate is initially zero and increases with time, implying that foundering begins when its growth rate is about equal to that of the pile. Theoretical models suggest that cumulates can grow rapidly in early stages of reservoir evolution due to convection [*Worster et al.*, 1990], so that evaluating all the different possibilities will require a range of theoretical and experimental studies. For the viscosity estimates and intrusion volumes that will be obtained below, the characteristic time of country rock deformation is typically 1 Myr or more. This is of the same order of magnitude as the typical duration of magmatic and volcanic activity in active areas. This indicates that spreading and foundering are not faster than intrusion growth and crystallization, allowing a separation between emplacement and postemplacement phases.

6.2. The Effective Viscosity of Host Rocks

The almost perfect circular outline of the large Sept-Iles intrusion (Figure 2) is best explained by lateral spreading away from a central feeder zone. It does not provide incontrovertible evidence for a viscous rheology, but other deformation mechanisms are highly unlikely for such a large body, as shown by *Jellinek and DePaolo* [2003]. One could appeal to some tectonic accommodation process, with magma intrusion compensating for

part of remotely induced large-scale deformation. This would be difficult to reconcile with the intrusion setting, however, which is the initiation of the St. Lawrence rift system and the opening of the Iapetus Ocean about 560 Myr ago [*Higgins and van Breemen*, 1998]. The intrusion is not elongated in any preferential direction and stretches over a large distance of about 80 km in a direction perpendicular to the rift.

The dimensionless number *Ai* depends on the various densities involved and on the intrusion volume, which can be determined with small uncertainties in most cases. It also depends on the viscosity of encasing material, which is not well known. Equation (6) relates *Ai* to the final aspect ratio of the intrusion, which can be measured easily and hence leads to constraints on viscosity. We restrict the analysis to those intrusions that are consistent with spreading away from a central feeder zone, such that they extend in all directions over similar distances, which include the Ardnamurchan, Rum, Sept-Iles, and Bushveld (Table 1). Values of *Ai* are bracketed by 10^1 (for the Ardnamurchan intrusion) and 3×10^5 (for the Bushveld Complex). Using these values, an initial density contrast $\Delta\rho_T$ of 25 kg m^{-3} and the volumes of Table 1, we obtain viscosities in the 10^{17} – 10^{18} Pa s range. Allowing for uncertainties in the volumes and the initial density difference would not change these order of magnitude estimates. The Ardnamurchan intrusion, with its aspect ratio of about 1, has probably not been affected by much spreading and can only provide a minimum viscosity value of 10^{18} Pa s. For such a relatively small intrusion, one may indeed expect that magmatic activity was not sustained for very long, implying little heating of encasing rocks.

The above viscosity values are consistent with the flow laws of crustal rocks at ambient temperatures in a 450–750°C range (Figure 3). Selecting one particular rock type as representative of the crust is far from obvious, and it is desirable to obtain direct viscosity estimates from field observations. In geological settings with little or no plutonic activity, the amplitude and pattern of lacustrine shoreline modifications induced by elevation or climate changes indicate viscosities in a range of 10^{19} – 10^{21} Pa s below a thin elastic upper layer [*Bills et al.*, 1994; *England et al.*, 2013]. Such studies have been carried out in areas where crustal temperatures are lower than in magmatic provinces and address the response of the crust to loads that are smaller than those involved here. They therefore provide upper bounds on viscosity values for our model. Estimates for active volcanic areas have been deduced from observations on magma replenishment events. For example, the Long Valley Caldera, California, experienced surface deformation over 8–10 months in 1997–1998 with a simple time-dependent pattern of exponential increase segueing into exponential decay [*Newman et al.*, 2001]. For a good fit to the data, wall rocks at a depth of about 6 km had to deform in a viscoelastic regime with viscosity in a 10^{15} – 10^{18} Pa s range. The different viscosity estimates must be compared with caution owing to the nonlinearity of the flow laws but, given the rather large ranges of values that are indicated, are consistent with one another.

6.3. Comparison With a Few Mafic Intrusions

The jellyfish and annular instabilities share two important characteristics that set them apart from the teardrop instability. They are characterized by thinning in the central part of the intrusion and thickening in an outer ring. This is the exact opposite of the teardrop instability, which sees thickening in the central region and the growth of a single axial downwelling. In geological conditions, where encasing rocks have a finite strength and flow laws that are strongly temperature dependent, the instability development is hampered and eventually stopped by the cooling of both the intrusion and its surroundings. The end result is a stable residual body that is available for inspection long after the event, which is not allowed by the present experiments. Such conditions have been investigated using numerical calculations for brittle-elastic-ductile deformation in a companion paper [*Roman and Jaupart*, 2016]. These calculations confirm the key role of the intrusion aspect ratio and reproduce the two contrasting behaviors that we have just described. They further show how teardrop intrusions can get frozen in the funnel-shaped bodies that are frequently observed in the field. The exact time at which deformation stops and the final shape of the mafic body that is achieved depend on the ambient thermal structure of the crust prior to intrusion as well as on the intrusion volume.

At one end of the spectrum, the Ardnamurchan and Rum intrusions, with their aspect ratios of about 1 and 0.5, belong to the teardrop category. They are characterized by the sagging of their floors associated with thickening at the center and inward dipping side walls. A preliminary gravity study suggests that the Rum intrusion extends to a depth of about 15 km in a relatively narrow axial region [*Emeleus et al.*, 1996], which would be consistent with the development of a funnel structure.

At the other end of the spectrum, the Bushveld Complex, with its very small aspect ratio, should be in the jellyfish or annular regimes, and there is some evidence that this is indeed the case. The present-day

exposure is discontinuous and made of four lobes (Figure 2). According to early geophysical models, the lobes are independent bodies that are not connected to one another [*Du Plessis and Kleywegt*, 1987; *Meyer and De Beer*, 1987]. One seemingly strong argument was that a continuous mafic body would have generated a positive gravity anomaly in the central area, for which there is no evidence. This interpretation, however, is difficult to reconcile with the nearly identical igneous layered series that are observed in the eastern and western lobes [*Cawthorn and Webb*, 2001]. Part of the problem lied with the limited depth extent of early geophysical models, which did not encompass the base of the crust. For the dimensions of the Bushveld Complex (>300 km), a no net large-wavelength gravity anomaly must be evaluated at the scale of the whole crust because Airy compensation can be achieved with a deep Moho. Seismic studies have indeed provided evidence for anomalously thick crust beneath the complex [*Webb et al.*, 2004; *Kgaswane et al.*, 2012]. Confirmation for the continuity between the eastern and western lobes was provided by xenolith suites from a kimberlite pipe and by drill holes [*Cawthorn and McKenna*, 2006; *Webb et al.*, 2011; *Cole et al.*, 2014]. It is now clear that the complex is thin in the center and thick at the edges (Figure 2). In addition, the central region has two striking features. There, the layered mafic series are locally interrupted by protrusions of Transvaal sedimentary basement [*Uken and Watkeys*, 1997; *Scoon*, 2002; *Cole et al.*, 2014]. Furthermore, it is lacking basal cumulates of the Lower Zone [*Webb et al.*, 2011; *Cole et al.*, 2014]. These features are strongly reminiscent of the jellyfish pattern, with a thin and lumpy central region, thick peripheral lobes, and an irregular planform (Figure 6). Interestingly, magnetic studies have shown that the dips of the Bushveld igneous layers were acquired below a Curie temperature of ≈580°C [*Letts et al.*, 2009], i.e., in a postcrystallization phase.

The Sept-Iles intrusion, with its small aspect ratio, would be in the jellyfish or annular categories if the instability had had time to develop, but, on the basis of current information, this apparently did not happen. This can be attributed to early freezing, but it may also be that the tell-tale features of an incipient foundering process, which would be most distinctive at the base of the intrusion, cannot be resolved by current data. Most of the intrusion lies beneath the Saint-Lawrence River, and outcrops and drill holes are only available at its northern edge. The rather coarse gravity data coverage is only sensitive to the large-scale intrusion shape and allows little information on either the composition (through density) of basal layers or irregularities of the floor [*Loncarevic et al.*, 1990; *Dion et al.*, 1998]. A few peculiar features of this intrusion indicate that it is not as simple as it appears to be. Its upper part hosts a few large gabbro bodies, whose vertical extensions have not been determined reliably [*Loncarevic et al.*, 1990; *Dion et al.*, 1998] and whose origin has not been ascertained. Furthermore, it seems to be missing the basal ultramafic bronzitic and peridotitic cumulates that are well developed in similar intrusions such as the Bushveld and the Stillwater, USA [*Dion et al.*, 1998].

6.4. Implications

According to this study, the thickness of an intrusion may not be set at the emplacement stage and may change as magma is crystallizing. It is also likely to be modified further past its magmatic phase when it is almost solid. The transition between the two main instability regimes, teardrop and "annular-jellyfish," occurs at a threshold aspect ratio of about 0.4, corresponding to a *Ai* value of ≈500 (Figure 10). For typical density values ($\Delta\rho_T = 25$ kg m^{-3}), this can be turned into a threshold relationship between the intrusion volume and the viscosity of surrounding rocks (Figure 12). For given volume and flow law, the teardrop regime requires viscosities above a critical value, corresponding to ambient temperatures below a critical value, with an exact value that depends on the flow law. This suggests that funnel-shaped intrusions are not likely to form in the lower crust unless their volumes are smaller than those that have been found in the upper crust. By the same token, intrusions should be mostly sill like deep in the crust. Thus, one expects the crust to be layered in terms of intrusion shapes.

That intrusions have been deformed significantly in a postemplacement phase is likely to affect how we interpret their internal igneous structures. This deserves an independent analysis, and in the interest of time, we only discuss briefly the particular case of funnel-shaped layered intrusions such as the Great Dyke of Zimbabwe. Most of these intrusions have grown out of elongated feeder zones analogous to rifts environments and hence cannot be compared directly to the present experiments. The same rather simple geometrical rules apply, however. In these intrusions, as summarized by *Latypov* [2015], an angular unconformity separates the basal "reversal" series and the evolved layered sequence along their steeply inclined walls. Their igneous layers dip at high angles and are almost vertical in the Jimberlana intrusion, Western Australia [*Campbell*, 1978]. Yet their cumulates exhibit rhythmic layering and textures that are identical to those from intrusions with

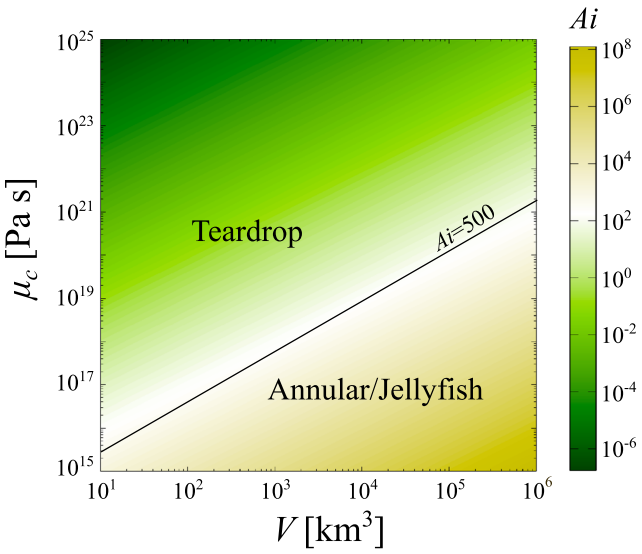


Figure 12. *Ai* as a function of intrusion volume and effective viscosity of encasing rocks. A reference value of $\Delta\rho_T = 25$ kg m^{-3} has been used for this calculation. The dashed line corresponds to $Ai = 500$, which marks the transition between the teardrop and the annular/jellyfish domains.

semihorizontal floors. This is seemingly at odds with physical models of cumulate formation, which rely on gravity-driven processes such as crystal settling, compaction, and compositional convection. The problem disappears if one allows for postcrystallization deformation. *Roman and Jaupart* [2016] have shown how igneous layers behave as an initially flat intrusion deforms into a funnel-shaped body. As the side walls steepen, these layers follow the general deformation, but contacts between individual layers get displaced leading to apparent unconformities along the walls. The layers thicken markedly toward the axial zone in the upper part of the intrusion and may be almost vertical in its lower part.

7. Conclusion

Laboratory experiments document the postemplacement behavior of intrusions that spread at a density interface and that undergo a buoyancy reversal due to cooling. Although they are undoubtedly simpler than geological reality, they illustrate the consequences of the formation of thick dense cumulate piles and the changes of intrusion shape that are induced. The foundering of dense cumulates proceeds in different dynamical regimes and takes different forms depending on the aspect ratio of the intrusion, which is itself a result of the spreading process. The most important control variables are the intrusion volume and the effective viscosity of surrounding rocks. Both variables are involved in a dimensionless number that allows prediction of the intrusion aspect ratio. Small viscosity values favor the formation of elongated bodies with small aspect ratios.

A range of intrusion shapes may be generated. In strong encasing rocks,intrusions are not likely to spread and deform significantly in strong encasing rocks, leading only to sagging in a central region. In weak surrounding rocks, small volume intrusions that do not extend over large distances founder in a teardrop regime characterized by thickening in a central region and a downward pointing funnel. For larger intrusions and weak surroundings, the deformation pattern is completely different, with thickening at the edge, thinning at the center, and the growth of peripheral lobes.

Crustal environments that are already hot when an intrusion forms will favor spreading and foundering and furthermore completion of the foundering process, as shown in *Roman and Jaupart* [2016]. If foundering does not proceed to completion, we expect the residual intrusion to be in a jellyfish/annular arrangement. From the perspective of global crust stratification, which goes from cold to hot with increasing depth, we expect that spreading is limited in the upper crust save for exceptional circumstances involving very large magma volumes, such as in the Sept-Iles and Bushveld cases, and efficient in the lower crust. Thus, the teardrop sagging regime should dominate in the upper crust and lower crustal regions should preserve mostly elongated sill-like lenses with thicker outer lobes.

Appendix A: Experimental Setup

Hot fluid was injected through a circular nozzle connected to a motor-powered calibrated syringe, which allowed control on the fluid volume. The intruding fluid was heated in the syringe prior to intrusion using a heating mat, which allowed a uniform temperature.

The three different fluids of each experiment were miscible, so that no surface tension effects were involved. In order to vary viscosity and density, we diluted Natrosol© hydroxyethylcellulose (varying between 0 and 1% concentration) and salt in distilled water. Natrosol solutions behave as Newtonian fluids at the strain rates of our experiments [*Tait and Jaupart*, 1989]. Viscosity values were measured with a stress-controlled rheometer with an uncertainty of less than 10%.

In order to visualize the flow, we diluted food dye in the fluids. Measurements were made on digital photographs taken every 5 s from the top. A grid was placed at the injection level once the experiments were finished in order to transform camera coordinates to real ones and to avoid aberrations due to lens and refraction at the fluid/air interface. The procedure has an accuracy of about 1%.

Acknowledgments
We thank Angela Limare for her critical and gentle assistance in the laboratory. The manuscript was improved very significantly by the incisive and positive reviews of Steve Sparks and Boris Kaus. The authors acknowledge financial support from the French National Program for Planetary Science (PNP) funded by CNRS-INSU and CNES. The data for this paper are available by contacting the corresponding author at roman@ipgp.fr.

References

Annen, C., and R. S. J. Sparks (2002), Effects of repetitive emplacement of basaltic intrusions on thermal evolution and melt generation in the crust, *Earth Planet. Sci. Lett.*, *203*(3), 937–955.
Annen, C., J. Blundy, and R. Sparks (2006), The genesis of intermediate and silicic magmas in deep crustal hot zones, *J. Petrol.*, *47*(3), 505–539.
Arndt, N. T., and S. L. Goldstein (1989), An open boundary between lower continental crust and mantle: Its role in crust formation and crustal recycling, *Tectonophysics*, *161*, 201–212, doi:10.1016/0040-1951(89)90154-6.
Asimow, P. D., and M. S. Ghiorso (1998), Algorithmic modifications extending MELTS to calculate subsolidus phase relations, *Am. Mineral.*, *83*, 1127–1132.
Bills, B. G., D. R. Currey, and G. A. Marshall (1994), Viscosity estimates for the crust and upper mantle from patterns of lacustrine shoreline deformation in the Eastern Great Basin, *J. Geophys. Res.*, *99*, 22,059–22,086, doi:10.1029/94JB01192.
Blackwell, D. D., J. L. Steele, S. Kelley, and M. A. Korosec (1990), Heat flow in the state of Washington and thermal conditions in the Cascade Range, *J. Geophys. Res.*, *95*(B12), 19,495–19,516.
Burchardt, S., V. R. Troll, L. Mathieu, H. C. Emeleus, and C. H. Donaldson (2013), Ardnamurchan 3D cone-sheet architecture explained by a single elongate magma chamber, *Sci. Rep.*, *3*, 2891.
Campbell, I. (1978), Some problems with the cumulus theory, *Lithos*, *11*(4), 311–323.
Cawthorn, R., and N. McKenna (2006), The extension of the western limb, Bushveld Complex (South Africa), at Cullinan Diamond Mine, *Mineral. Mag.*, *70*(3), 241–256.
Cawthorn, R., and S. Webb (2001), Connectivity between the western and eastern limbs of the Bushveld Complex, *Tectonophysics*, *330*(3), 195–209.
Cawthorn, R. G. (2015), The Bushveld Complex, South Africa, in *Layered Intrusions*, edited by B. Charlier et al., pp. 517–587, Springer, Netherlands.
Cawthorn, R. G., and F. Walraven (1998), Emplacement and crystallization time for the Bushveld Complex, *J. Petrol.*, *39*(9), 1669–1687.
Christensen, N., and W. Mooney (1995), Seismic velocity structure and composition of the continental crust: A global view, *J. Geophys. Res.*, *100*, 9761–9788.
Cole, J., S. J. Webb, and C. A. Finn (2014), Gravity models of the Bushveld Complex—Have we come full circle?, *J. Afr. Earth. Sci.*, *92*, 97–118.
Del Negro, C., G. Currenti, and D. Scandura (2009), Temperature-dependent viscoelastic modeling of ground deformation: Application to Etna volcano during the 1993–1997 inflation period, *Phys. Earth Planet. Inter.*, *172*(3), 299–309.
Dion, D. J., K. Authier, J. Cimon, and T. Feininger (1998), Le complexe de sept-iles: II—Interpretation gravimetrique du complexe mafique stratifie, *Tech. Rep. ET97-05*, Ministere de l'Energie et des Resources du Quebèc.
Du Plessis, A., and R. Kleywegt (1987), A dipping sheet model for the mafic lobes of the Bushveld Complex, *S. Afr. J. Geol.*, *90*(1), 1–6.
Emeleus, C. H., and V. R. Troll (2014), The Rum Igneous Centre, Scotland, *Mineral. Mag.*, *78*, 805–839, doi:10.1180/minmag.2014.078.4.04.
Emeleus, C. H., M. J. Cheadle, R. H. Hunter, B. G. J. Upton, and W. J. Wadsworth (1996), The Rum layered suite, *Dev. Petrol.*, *15*, 403–439.
England, P. C., R. T. Walker, B. Fu, and M. A. Floyd (2013), A bound on the viscosity of the Tibetan crust from the horizontality of palaeolake shorelines, *Earth Planet. Sci. Lett.*, *375*, 44–56, doi:10.1016/j.epsl.2013.05.001.
Ghiorso, M. S., and R. O. Sack (1995), Chemical mass transfer in magmatic processes: IV. A revised and internally consistent thermodynamic model for the interpolation and extrapolation of liquid-solid equilibria in magmatic systems at elevated temperatures and pressures, *Contrib. Mineral. Petrol.*, *119*(2–3), 197–212.
Glazner, A. F., J. M. Bartley, D. S. Coleman, W. Gray, and R. Z. Taylor (2004), Are plutons assembled over millions of years by amalgamation from small magma chambers, *GSA Today*, *14*, 1099, doi:10.1130/1052-5173(2004)014.
Higgins, M. D., and O. van Breemen (1998), The age of the Sept Iles layered mafic intrusion, Canada: Implications for the Late Neoproterozoic/Cambrian History of Southeastern Canada, *J. Geol.*, *106*, 421–432, doi:10.1086/516033.
Hirose, K., and I. Kushiro (1993), Partial melting of dry peridotites at high pressures: Determination of compositions of melts segregated from peridotite using aggregates of diamond, *Earth Planet. Sci. Lett.*, *114*(4), 477–489.
Holness, M., M. Hallworth, A. Woods, and R. Sides (2007), Infiltration metasomatism of cumulates by intrusive magma replenishment: The Wavy Horizon, Isle of Rum, Scotland, *J. Petrol.*, *48*(3), 563–587.
Irvine, T. N. (1970), Crystallization sequences in the Muskox intrusion and other layered intrusions: I. Olivine-pyroxene-plagioclase relations, *Geol. Soc. S. Africa Spec. Publ.*, *1*(7478), 441–476.
Jellinek, A. M., and D. J. DePaolo (2003), A model for the origin of large silicic magma chambers: Precursors of caldera-forming eruptions, *Bull. Volcanol.*, *65*, 363–381, doi:10.1007/s00445-003-0277-y.
Jull, M., and P. Kelemen (2001), On the conditions for lower crustal convective instability, *J. Geophys. Res.*, *106*(B4), 6423–6446.
Kay, R., and S. Mahlburg-Kay (1991), Creation and destruction of lower continental crust, *Geol. Rundsch.*, *80*(2), 259–278.

Kgaswane, E. M., A. A. Nyblade, R. J. Durrheim, J. Julià, P. H. Dirks, and S. J. Webb (2012), Shear wave velocity structure of the Bushveld Complex, South Africa, *Tectonophysics*, *554*, 83–104.
Koch, D. M., and D. L. Koch (1995), Numerical and theoretical solutions for a drop spreading below a free fluid surface, *J. Fluid Mech.*, *287*, 251–278, doi:10.1017/S0022112095000942.
Kohlstedt, D., B. Evans, and S. Mackwell (1995), Strength of the lithosphere: Constraints imposed by laboratory experiments, *J. Geophys. Res.*, *100*, 17,587–17,602.
Latypov, R. (2015), Basal reversals in mafic sills and layered intrusions, in *Layered Intrusions*, edited by B. Charlier et al., pp. 259–293, Springer, Netherlands.
Letts, S., T. H. Torsvik, S. J. Webb, and L. D. Ashwal (2009), Palaeomagnetism of the 2054 Ma Bushveld Complex (South Africa): Implications for emplacement and cooling, *Geophys. J. Int.*, *179*(2), 850–872.
Lister, J. R., and R. C. Kerr (1989a), The propagation of two-dimensional and axisymmetric viscous gravity currents at a fluid interface, *J. Fluid Mech.*, *203*, 215–249, doi:10.1017/S0022112089001448.
Lister, J. R., and R. C. Kerr (1989b), The effect of geometry on the gravitational instability of a buoyant region of viscous fluid, *J. Fluid Mech.*, *202*, 577–594, doi:10.1017/S0022112089001308.
Loncarevic, B. D., T. Feininger, and D. Lefebvre (1990), The Sept-îles layered mafic intrusion: Geophysical expression, *Can. J. Earth Sci.*, *27*, 501–512, doi:10.1139/e90-046.
Manga, M., et al. (2012), Heat flow in the Lesser Antilles island arc and adjacent back arc Grenada basin, *Geochem. Geophys. Geosyst.*, *13*, Q08007, doi:10.1029/2012GC004260.
Masterlark, T., M. Haney, H. Dickinson, T. Fournier, and C. Searcy (2010), Rheologic and structural controls on the deformation of Okmok volcano, Alaska: FEMs, InSAR, and ambient noise tomography, *J. Geophys. Res.*, *115*, B02409, doi:10.1029/2009JB006324.
McClay, K., and I. Campbell (1976), The structure and shape of the Jimberlana intrusion, Western Australia, as indicated by an investigation of the Bronzite Complex, *Geol. Mag.*, *113*(2), 129–139.
Meyer, R., and J. De Beer (1987), Structure of the Bushveld Complex from resistivity measurements, *Nature*, *325*, 610–612.
Michaut, C. (2011), Dynamics of magmatic intrusions in the upper crust: Theory and applications to laccoliths on Earth and the Moon, *J. Geophys. Res.*, *116*, B05205, doi:10.1029/2010JB008108.
Michaut, C., and C. Jaupart (2006), Ultra-rapid formation of large volumes of evolved magma, *Earth Planet. Sci. Lett.*, *250*(1), 38–52.
Morse, S. A. (2015), Kiglapait Intrusion, Labrador, in *Layered Intrusions*, edited by B. Charlier et al., pp. 589–648, Springer, Netherlands.
Namur, O., B. Charlier, M. J. Toplis, M. D. Higgins, J.-P. Liégeois, and J. Vander Auwera (2010), Crystallization sequence and magma chamber processes in the ferrobasaltic Sept iles layered intrusion, Canada, *J. Petrol.*, *51*(6), 1203–1236.
Newman, A. V., T. H. Dixon, G. I. Ofoegbu, and J. E. Dixon (2001), Geodetic and seismic constraints on recent activity at Long Valley Caldera, California: Evidence for viscoelastic rheology, *J. Volcanol. Geotherm. Res.*, *105*, 183–206, doi:10.1016/S0377-0273(00)00255-9.
O'Driscoll, B., V. Troll, R. Reavy, and P. Turner (2006), The Great Eucrite intrusion of Ardnamurchan, Scotland: Reevaluating the ring-dike concept, *Geology*, *34*(3), 189–192.
Podmore, F., and A. Wilson (1987), A reappraisal of the structure, geology and emplacement of the Great Dyke, Zimbabwe, in *Mafic Dyke Swarms, Geol. Assoc. Canada Spec. Pap.*, vol. 34, edited by H. C. Halls and W. F. Fahrig, pp. 317–330, Geol. Assoc. Canada, St John's, Newfoundland.
Ranalli, G. (1995), *Rheology of the Earth*, Springer Science and Business Media, Netherlands.
Ranalli, G., and D. C. Murphy (1987), Rheological stratification of the lithosphere, *Tectonophysics*, *132*(4), 281–295.
Roman, A., and C. Jaupart (2016), The fate of mafic and ultramafic intrusions in the continental crust, *Earth Planet. Sci. Lett.*, *453*, 131–140.
Rudnick, R. L., and D. M. Fountain (1995), Nature and composition of the continental crust: A lower crustal perspective, *Rev. Geophys.*, *33*, 267–309, doi:10.1029/95RG01302.
Scoon, R. N. (2002), A new occurrence of Merensky Reef on the flanks of the Zaaikloof dome, northeastern Bushveld Complex: Relationship between diapirism and magma replenishment, *Econ. Geol.*, *97*(5), 1037–1049.
Sisson, T. W., T. L. Grove, and D. S. Coleman (1996), Hornblende gabbro sill complex at Onion Valley, California, and a mixing origin for the Sierra Nevada batholith, *Contrib. Mineral. Petrol.*, *126*, 81–108.
Springer, M., and A. Förster (1998), Heat-flow density across the Central Andean subduction zone, *Tectonophysics*, *291*(1), 123–139.
Taisne, B., and C. Jaupart (2009), Dike propagation through layered rocks, *J. Geophys. Res.*, *114*, B09203, doi:10.1029/2008JB006228.
Tait, S., and C. Jaupart (1989), Compositional convection in viscous melts, *Nature*, *338*, 571–574.
Uken, R., and M. K. Watkeys (1997), Diapirism initiated by the Bushveld Complex, South Africa, *Geology*, *25*(8), 723–726.
Wager, L. R., and G. M. Brown (1968), *Layered Igneous Rocks*, Oliver and Boyd, Edinburgh and London.
Webb, S. J., R. G. Cawthorn, T. Nguuri, and D. James (2004), Gravity modeling of Bushveld Complex connectivity supported by Southern African seismic experiment results, *S. Afr. J. Geol.*, *107*(1–2), 207–218.
Webb, S. J., L. D. Ashwal, and R. G. Cawthorn (2011), Continuity between eastern and western Bushveld Complex, South Africa, confirmed by xenoliths from kimberlite, *Contrib. Mineral. Petrol.*, *162*(1), 101–107.
Wilson, A. (1996), The great dyke of Zimbabwe, *Dev. Petrol.*, *15*, 365–402.
Worster, M. G., H. E. Huppert, R. Stephen, and J. Sparks (1990), Convection and crystallization in magma cooled from above, *Earth Planet. Sci. Lett.*, *101*, 75–89.
Yudovskaya, M. A., A. J. Naldrett, J. A. Woolfe, G. Costin, and J. A. Kinnaird (2015), Reverse compositional zoning in the Uitkomst chromitites as an indication of crystallization in a magmatic conduit, *J. Petrol.*, *56*, 2373–2394.